EPJ Plus

EPJ.org
your physics journal

Eur. Phys. J. Plus (2018) **133**: 338 DOI 10.1140/epjp/i2018-12154-3

Giant enhancement of second harmonic generation efficiency from MoS_2 mono layers embedded in 1D photonic crystals

M. Khani, M. Khazaei Nezhad and H. Rastegar Moghaddam Rezaeiun

Società Italiana di Fisica

Springer

Eur. Phys. J. Plus (2018) **133**: 338
DOI 10.1140/epjp/i2018-12154-3

THE EUROPEAN PHYSICAL JOURNAL PLUS

Regular Article

Giant enhancement of second harmonic generation efficiency from MoS_2 mono layers embedded in 1D photonic crystals

M. Khani, M. Khazaei Nezhad[a], and H. Rastegar Moghaddam Rezaeiun

Department of Physics, Faculty of Sciences, Ferdowsi University of Mashhad, Mashhad, Iran

Received: 5 May 2018 / Revised: 18 July 2018
Published online: 24 August 2018

Abstract. In this paper an enhancement of second harmonic generation efficiency which radiated from MoS_2 monolayers embedded in one-dimensional photonic crystal structures is studied. The system contains air, SiO_2 and MoS_2 layers in periodic manner with the same thickness of air and SiO_2 layers. The transfer matrix method is used for calculating the forward and backward second harmonic generated wave efficiencies in undepleted pump approximation. Our results show the giant enhancement of second harmonic generation efficiencies up to seven orders of magnitude only with $N = 40$ MoS_2 monolayers in the system. The results are obtained by tunning the thickness of air and SiO_2 layers at about 1284 nm for fundamental wave of $\lambda = 810$ nm wavelength. Choosing the above thickness causes the second harmonic waves, generated in each MoS_2 monolayers, to interference constructively. Both of the fundamental and second harmonic wavelengths are located at the photonic band gap edges where the density of electromagnetic modes and the nonlinear interaction time are enhanced. These two mechanisms help us to improve the second harmonic generation efficiencies. Increasing the segments numbers enhanced the overall thickness of MoS_2 nonlinear layers which affect the phase matching conditions and decreased the SH efficiencies.

1 Introduction

The discovery of graphene monolayers in recent years has shown that some 2D materials have different behavior than its bulk state [1,2]. One of the most important group of these materials is known as transition-metal dichalcogenides (TMDs) monolayers in which one of the transition metal atom, such as Mo and W sandwiched between two chalcogene atoms such as S, Se and Te in hexagonal structure [3–9]. The materials in the bulk state have indirect band gap with inversion symmetry of crystalline structure [3–6]. The crystalline inversion symmetry decreases the second-order nonlinear optical effects such that the second-order susceptibility ($\chi^{(2)}$) of these materials is about $10^{-14}\ \frac{\mathrm{m}}{\mathrm{V}}$ in the bulk state [10–20]. Decreasing the dimension, the 2D monolayer of TMDs behave similar to the semiconductors with direct band gap. Also the crystalline inversion symmetry is broken [3–9,11–20]. Absence of the inversion symmetry enhances the second-order nonlinear optical effects [10–20]. The materials can be fabricated with various methods, such as the chemical vapor deposition (CVD) or mechanically exfoliation on the silicon substrates [10–20]. Based on the fabrication methods, $\chi^{(2)}$ can be enhanced up to $10^{-7}\ \frac{\mathrm{m}}{\mathrm{V}}$ [10]. The thickness of TMDs are about 0.65 nm [10–20]. One of the most investigated of TMDs is molybdenum disulfide (MoS_2) monolayers. Few layers of MoS_2 shows excellent linear and nonlinear optical effects such as strong photoluminescence, ultrafast carrier dynamics, saturable absorption and bandgap tuning by varying the number of layers [3,6–11,13,15,17]. Also, the second harmonic waves from some of 2DTMDs were observed recently when subjected under the Ti:saphare laser radiations with 810 nm wavelength [10–20]. Although decreasing the dimension of TMDs enhances the second order nonlinear optical coefficient but insignificant thickness of TMDs monolayers diminishes second harmonic generation (SHG) efficiency in comparison with the popular nonlinear crystals such as KDP, BBO and SBN [21–24].

The aim of this paper is enhancement of second harmonic (SH) efficiency from molybdenum disulfide monolayers by embedding them in the finite 1D photonic crystal structures. The 1D photonic crystals consist of at least two material layers with different refractive index which arranged in a periodic manner and affect the photons motion in similar way that crystalline lattices affect the electrons in solid state physics [25–27]. There are some mechanisms to

[a] e-mail: khazaeinezhad@um.ac.ir

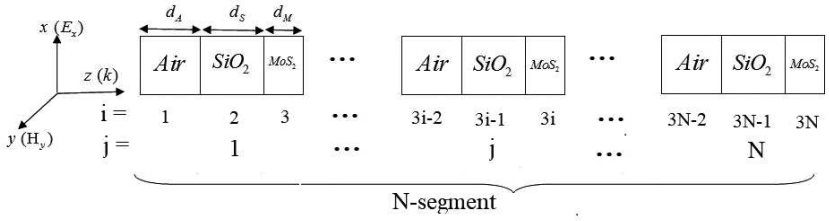

Fig. 1. Finite 1D photonic crystal arrangement.

assistance the process such as external feedback, defective mode, band gap tailoring and quasi-phase matching [21–24]. In some experimental works, the above mechanisms are applied to enhance the SHG efficiency of 2DTMD layers [15, 19, 28]. Here we concentrate to the phase matching of generated second harmonic waves from different MoS_2 layers by tuning the thickness of dielectric materials between them that used in 1D photonic crystal structure. The study was done using the transfer matrix method (TMM) [21–24]. This process causes the giant enhancement of SHG efficiency up to seven orders of magnitude for forward and backwared SH waves with only 40 MoS_2 monolayers. We hope these structures can be used as a component of nano photonic circuits and nonlinear light sources.

The paper is organized in four sections. In sect. 2, the 1D photonic crystal and the transfer matrix method are introduced. Numerical results and discussion are presented in sect. 3. Finally, we summarized our results in sect. 4.

2 Theoretical model

To observe the second harmonic waves from MoS_2 monolayers in recent works, the layers are deposited on the silica substrates [10–20]. We construct the finite 1D photonic crystal by these two components and the air films as $(\mathrm{Air}/\mathrm{SiO_2}/\mathrm{MoS_2})^N$, with the thickness of d_A, d_S and d_M for Air, SiO_2 and MoS_2 layers, respectively, where N is the number of segments (see fig. 1).

We use the Hybrid Lorentz-Drude-Gaussian model with 6 resonance frequencies to define the complex relative electric permittivity of the MoS_2 mono layers as: $\varepsilon_M = \varepsilon_M^{LD} + \varepsilon_M^G$ [7–9]. The Lorentz-Drude part of the frequency-dependent electric permittivity is given by [7–9]

$$\varepsilon_M^{LD}(\omega) = \varepsilon_\infty + \sum_{j=0}^{5} \frac{S_j \omega_P^2}{\omega_j^2 - \omega^2 - i\Gamma_j \omega}\,, \tag{1}$$

where, ω_P is the plasma frequency, ε_∞ is the background or DC permittivity, ω_j, S_j and Γ_j are the resonance frequency, oscillator strength and the damping coefficient of the j-th resonance, respectively. The resonance frequencies are 0, 1.88, 2.03, 2.78, 2.91, 4.31 eV, the damping coefficients are 1.0853×10^{-2}, 5.9099×10^{-2}, 1.1302×10^{-1}, 1.1957×10^{-1}, 2.8322×10^{-1}, 7.8515×10^{-1} eV and the oscillator strengths are 2.0089×10^5, 5.7534×10^4, 8.1496×10^4, 8.2293×10^4, 3.3130×10^5, 4.3906×10^6, respectively. The plasma frequency of MoS_2 layer is $\frac{28.3}{2\pi}$ meV and the ε_∞ is 4.44 [7–9].

The imaginary part of the Gaussian component of the MoS_2 electric permittivity is given by [7]

$$\varepsilon_{iM}^G(\omega) = \alpha \exp\left(-\frac{(\hbar\omega - \mu)^2}{2\sigma^2}\right), \tag{2}$$

where $\alpha = 23.224$, $\mu = 2.7723$ eV and $\sigma = 0.3089$ eV, respectively. The real part of the Gaussian component of the MoS_2 electric permittivity can be obtained by using the Kramers-Kronig dispersion relation [7]

$$\varepsilon_{rM}^G(\omega) = 1 + \frac{1}{\pi} P.V. \int_{-\infty}^{\infty} \frac{\varepsilon_{iM}^G(\omega)'}{(\omega' - \omega)} \mathrm{d}\omega', \tag{3}$$

which leads to

$$\varepsilon_{rM}^G(\omega) = 1 - \frac{2\alpha}{\sqrt{\pi}} DF\left(\frac{(\hbar\omega - \mu)}{\sqrt{2}\sigma}\right); \tag{4}$$

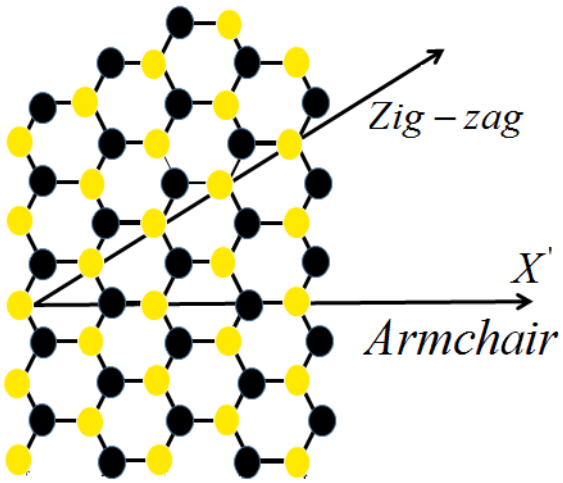

Fig. 2. Lattice structure of MoS_2 monolayer, black circles are S atoms and yellow circles show Mo atoms.

here, $DF(x)$ is the Dawson-Function of argument x. The refractive index and extinction coefficient of the MoS_2 mono layer are obtained from the overall complex electric permittivity as follows:

$$n_M(\omega) = \sqrt{\frac{1}{2}\left(\varepsilon_{rM} + \sqrt{\varepsilon_{rM}^2 + \varepsilon_{iM}^2}\right)},$$
$$K_M(\omega) = \sqrt{\frac{1}{2}\left(-\varepsilon_{rM} + \sqrt{\varepsilon_{rM}^2 + \varepsilon_{iM}^2}\right)}. \tag{5}$$

Also, the refractive index of SiO_2 films are obtained as [29]

$$n_S(\lambda) = \sqrt{A + \frac{B\lambda^2}{\lambda^2 - C} + \frac{D\lambda^2}{\lambda^2 - 100}}, \tag{6}$$

where $A = 1.28604141$, $B = 1.07044083$, $C = 1.00585997 \times 10^{-2}$, $D = 1.10202242$ and λ is in nm unit [29]. The refractive index of air films set equal to one.

We assume that the interface of 1D photonic crystal components laid in the xy plane (see fig. 1). The fundamental wave (FW) of wavelength λ and electric field polarization along the x-axis is incident normally on the one dimensional nonlinear photonic crystal (1DNPC) that propagated along the z-direction.

The MoS_2 layer has hexagonal structure belong to the D_{3h} crystalline symmetry group and the second-order nonlinear susceptibility tensor has nonzero elements of [10]: $\chi^{(2)}_{y'y'y'} = -\chi^{(2)}_{y'x'x'} = -\chi^{(2)}_{x'x'y'} = -\chi^{(2)}_{x'y'x'}$, where x', y', z' are crystalline coordinates. Here x' is along the armchair direction (see fig. 2). In our 1D photonic crystal structure the incident beam is linearly polarized along the x-direction where the x-, y-, z-directions are shown in fig. 1 and known as lab coordinates. It can be shown that the parallel (x) and perpendicular (y) component of the SH electric field are proportional to $\sin 3\theta$ and $\cos 3\theta$, respectively, where θ is the angle between x (incident electric field direction) and x' (armchair direction of MoS_2 monolayers) [10]. Hence, if we adjust the $\theta = 30$, by rotating the incident light polarization, the SH electric field has only the parallel component and we can use the scalar equation with an effective susceptibility for generated second harmonic wave.

As known, in second-order nonlinear optical material such as MoS_2 monolayer, an incident wave of frequency ω (wavelength λ) can be converted to the second harmonic wave of frequency 2ω (wavelength of $\frac{\lambda}{2}$). In fact the incident wave acts as a source of second harmonic wave. Also, it is is possible that the generated second harmonic wave converted to the incident fundamental wave in the reverse process. Therefore, the second harmonic wave can also act as a source of fundamental wave. But if the incident light intensity is sufficiently large, the intensity of fundamental wave that generated in the reverse process can be neglected. This approximation is called the undepleted pump approximation.

In undepleted pump approximation the FW electric field $E_i^{(1)}(z)$ and the SH electric field $E_i^{(2)}(z)$ in the i-th layer satisfy the following equations [21–24]:

$$\frac{\mathrm{d}^2 E_i^{(1)}(z)}{\mathrm{d}z^2} + k_i^{(1)2} E_i^{(1)}(z) = 0, \tag{7}$$

$$\frac{\mathrm{d}^2 E_i^{(2)}(z)}{\mathrm{d}z^2} + k_i^{(2)2} E_i^{(2)}(z) = -k_{20}^2 \chi_i^{(2)} E_i^{(1)2}(z), \tag{8}$$

where $k_i^{(1)} = n_i^{(1)} k_{10}$, $k_i^{(2)} = n_i^{(2)} k_{20}$, $k_{20} = 2k_{10}$ and $k_{10} = \frac{\omega}{c}$. $n_i^{(1)}$ $[n_i^{(2)}]$ is the refractive index of the i-th layer material at the fundamental [SH] wave frequency. c is the speed of light in vacuum. $\chi_i^{(2)}$ is the second-order nonlinear optical coefficient of the i-th layer.

From eq. (7), the FW electric field in the i-th layer can be expanded with forward and backward plane waves in the z-direction as follows:

$$E_i^{(1)}(z) = \Omega_i^{(1)+} e^{ik_i^{(1)}(z - z_{i-1})} + \Omega_i^{(1)-} e^{-ik_i^{(1)}(z - z_{i-1})}. \tag{9}$$

Here, $\Omega_i^{(1)\pm}$ are the forward and backward FW electric field amplitudes at the beginning of the i-th layer. $z_i = z_{i-1} + d_i$, z_0 is set to zero and d_i is the thickness of the i-th layer. Applying the continuous conditions of electric and magnetic fields at each interface, we obtain

$$\begin{pmatrix} \Omega_i^{(1)+} \\ \Omega_i^{(1)-} \end{pmatrix} = t_i^{(1)} \begin{pmatrix} \Omega_{i-1}^{(1)+} \\ \Omega_{i-1}^{(1)-} \end{pmatrix}, \tag{10}$$

where $t_i^{(1)}$ is defined as [23]

$$t_i^{(1)} = D_0^{-1} D_i P_i D_i^{-1} D_0, \tag{11}$$

the related matrices are

$$D_0 = \begin{pmatrix} 1 & 1 \\ n_0 & -n_0 \end{pmatrix}, \qquad D_i = \begin{pmatrix} 1 & 1 \\ n_i^{(1)} & -n_i^{(1)} \end{pmatrix}, \qquad P_i = \begin{pmatrix} e^{ik_i^{(1)} d_i} & 0 \\ 0 & e^{-ik_i^{(1)} d_i} \end{pmatrix}, \tag{12}$$

where n_0 is the refractive index of the air background and is set equal to one. The overall T-matrix of the system can be calculated by successive products of individual transfer matrix t_i. The FW electric field amplitude in the left and right side of the structure is connected with the overall T-matrix as [21–24]

$$\begin{pmatrix} E_t^{(1)} \\ 0 \end{pmatrix} = T \begin{pmatrix} E_0 \\ E_r^{(1)} \end{pmatrix}. \tag{13}$$

Thus the reflected and transmitted FW electric field amplitude can be obtained as $E_r^{(1)} = -\frac{T_{21}}{T_{22}} E_0$, $E_t^{(1)} = \frac{|T|}{T_{22}} E_0$, where $|T|$ denotes the determinant of overall transfer matrix T. Also one can obtain forward and backward FW electric field amplitudes in each layer of our 1DNPC structure, that contains three components, as follows:

$$\begin{aligned}
\begin{pmatrix} \Omega_{3i-2}^{(1)+} \\ \Omega_{3i-2}^{(1)-} \end{pmatrix} &= D_A^{-1} t^{i-1} D_0 \begin{pmatrix} E_0 \\ E_r^{(1)} \end{pmatrix}, \\
\begin{pmatrix} \Omega_{3i-1}^{(1)+} \\ \Omega_{3i-1}^{(1)-} \end{pmatrix} &= D_S^{-1} (D_A P_A D_A^{-1}) t^{i-1} D_0 \begin{pmatrix} E_0 \\ E_r^{(1)} \end{pmatrix}, \\
\begin{pmatrix} \Omega_{3i}^{(1)+} \\ \Omega_{3i}^{(1)-} \end{pmatrix} &= D_M^{-1} (D_S P_S D_S^{-1}) (D_A P_A D_A^{-1}) t^{i-1} D_0 \begin{pmatrix} E_0 \\ E_r^{(1)} \end{pmatrix}.
\end{aligned} \tag{14}$$

$\Omega_{3i-k}^{(1)(\pm)}$ with $k = 0, 1, 2$ denote the forward and backward FW electric field amplitudes at the left-hand side of MoS_2 ($k = 0$), SiO_2 ($k = 1$) and air ($k = 2$) films in i-th segment, respectively (see fig. 1).

The sub-indexes A, S, M and 0 refer to the Air, SiO_2, MoS_2 and background medium, respectively. t is the one segment transfer matrix obtained from $t = (D_M P_M D_M^{-1})(D_S P_S D_S^{-1})(D_A P_A D_A^{-1})$.

After calculation of the fundamental electric and magnetic fields, we investigate the generation and propagation of second harmonic waves in our system. As known from eq. (8), the FW acts as a source of SH waves. By inserting the FW solution (eq. (9)) into eq. (8), one can obtain the SH electric field amplitude in i-th layer as follows:

$$E_i^{(2)}(z) = \Omega_i^{(2)+} e^{ik_i^{(2)}(z-z_{i-1})} + \Omega_i^{(2)-} e^{-ik_i^{(2)}(z-z_{i-1})} + A_i \left[\Omega_i^{(1)+}\right]^2 e^{2ik_i^{(1)}(z-z_{i-1})} + A_i \left[\Omega_i^{(1)-}\right]^2 e^{-2ik_i^{(1)}(z-z_{i-1})} + C_i \Omega_i^{(1)+} \Omega_i^{(1)-}, \tag{15}$$

where $\Omega_i^{(2)\pm}$ are forward and backward second harmonic electric field amplitudes at the beginning of the i-th layer and $A_i = -\frac{k_{20}^2 \chi_i^{(2)}}{(k_i^{(2)2} - 4k_i^{(1)2})}$, $C_i = -\frac{2k_{20}^2 \chi_i^{(2)}}{k_i^{(2)2}}$ [21–24].

Using Maxwell's equation as $\vec{\nabla} \times \vec{E}_i^{(2)}(z) = ik_{20}\vec{H}_i^{(2)}(z)$, we can derive the SH magnetic field as

$$H_i^{(2)}(z) = n_i^{(2)} \left(\Omega_i^{(2)+} e^{ik_i^{(2)}(z-z_{i-1})} - \Omega_i^{(2)-} e^{-ik_i^{(2)}(z-z_{i-1})}\right) + n_i^{(1)} \left(A_i \left[\Omega_i^{(1)+}\right]^2 e^{2ik_i^{(1)}(z-z_{i-1})} - A_i \left[\Omega_i^{(1)-}\right]^2 e^{-2ik_i^{(1)}(z-z_{i-1})}\right). \tag{16}$$

Applying the continuous conditions for SH electric and magnetic fields at each interface, one can acquire a relation between forward and backward SH electric field amplitudes at the $(i-1)$-th and i-th layers as follows [21–24]:

$$\begin{pmatrix} \Omega_i^{(2)+} \\ \Omega_i^{(2)-} \end{pmatrix} = t_i^{(2)} \begin{pmatrix} \Omega_{i-1}^{(2)+} \\ \Omega_{i-1}^{(2)-} \end{pmatrix} + \begin{pmatrix} r_i^+ \\ r_i^- \end{pmatrix}. \tag{17}$$

The applied matrices are given by [21–24]

$$t_i^{(2)} = G_0^{-1} N_i G_0, \qquad N_i = G_i Q_i G_i^{-1},$$
$$\begin{pmatrix} r_i^+ \\ r_i^- \end{pmatrix} = G_0^{-1} \left[(B_i F_i - N_i B_i) A_i \begin{pmatrix} \left[\Omega_i^{(1)+}\right]^2 \\ \left[\Omega_i^{(1)-}\right]^2 \end{pmatrix} + (1 - N_i) C_i \begin{pmatrix} \Omega_i^{(1)+} \Omega_i^{(1)-} \\ 0 \end{pmatrix} \right] \tag{18}$$

and

$$G_0 = \begin{pmatrix} 1 & 1 \\ n_0 & -n_0 \end{pmatrix}, \qquad G_i = \begin{pmatrix} 1 & 1 \\ n_i^{(2)} & -n_i^{(2)} \end{pmatrix}, \qquad B_i = \begin{pmatrix} 1 & 1 \\ 2n_i^{(1)} & -2n_i^{(1)} \end{pmatrix},$$
$$Q_i = \begin{pmatrix} e^{ik_i^{(2)} d_i} & 0 \\ 0 & e^{-ik_i^{(2)} d_i} \end{pmatrix}, \qquad F_i = \begin{pmatrix} e^{2ik_i^{(1)} d_i} & 0 \\ 0 & e^{-2ik_i^{(1)} d_i} \end{pmatrix}. \tag{19}$$

Using the above recursive relation, we obtain the following relation between the SH electric field amplitudes at the beginning of the j-th segment based on the $(j-1)$-th segment

$$\begin{pmatrix} \Omega_j^{(2)+} \\ \Omega_j^{(2)-} \end{pmatrix} = G_0^{-1} S_3 G_0 \begin{pmatrix} \Omega_{j-1}^{(2)+} \\ \Omega_{j-1}^{(2)-} \end{pmatrix} + G_0^{-1} \left\{ (S_2 B_A F_A - S_3 B_A) A_A \begin{pmatrix} \Omega_{3j-2}^{(1)+} \\ \Omega_{3j-2}^{(1)-} \end{pmatrix} + (S_2 - S_3) C_A \begin{pmatrix} \Omega_{3j-2}^{(1)+} \Omega_{3j-2}^{(1)-} \\ 0 \end{pmatrix} + (S_1 B_S F_S - S_2 B_S) A_S \begin{pmatrix} \Omega_{3j-1}^{(1)+} \\ \Omega_{3j-1}^{(1)-} \end{pmatrix} + (S_1 - S_2) C_S \begin{pmatrix} \Omega_{3j-1}^{(1)+} \Omega_{3j-1}^{(1)-} \\ 0 \end{pmatrix} + (B_M F_M - S_1 B_M) A_M \begin{pmatrix} \Omega_{3j}^{(1)+} \\ \Omega_{3j}^{(1)-} \end{pmatrix} + (1 - S_1) C_M \begin{pmatrix} \Omega_{3j}^{(1)+} \Omega_{3j}^{(1)-} \\ 0 \end{pmatrix} \right\}, \tag{20}$$

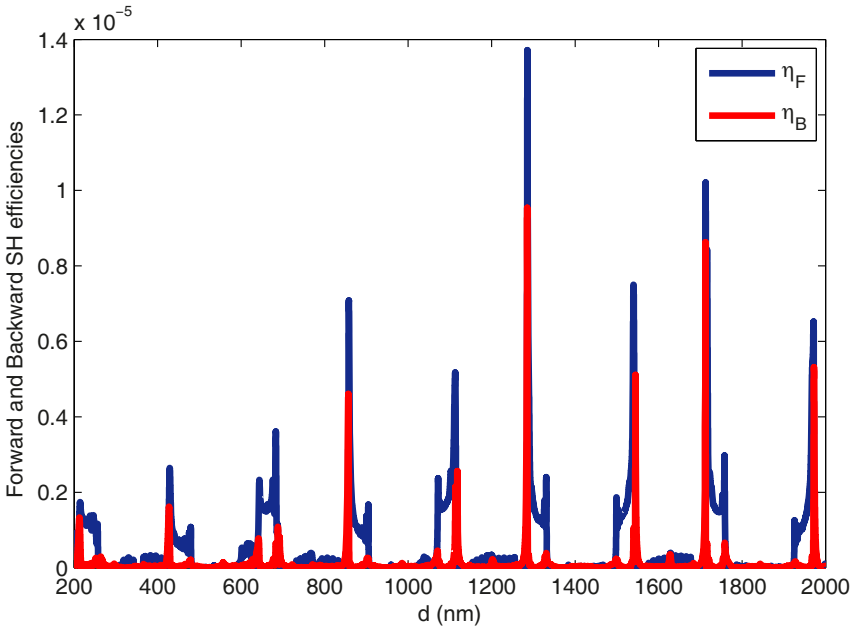

Fig. 3. Forward and backward SHG efficiencies *versus* the same thickness of air and SiO_2 layers for 1DNPC contains $N = 10$ segments.

where $S_1 = N_M$, $S_2 = N_M N_S$, $S_3 = N_M N_S N_A$. The above recursive relation can be served as the unit transfer matrix of the SH field for the j-th segment. Considering the periodicity of the structure and neglecting the nonlinear behavior of the air and SiO_2 films with respect to the MoS_2 mono layers ($\chi_A^{(2)} \cong 0, \chi_S^{(2)} \cong 0$), one can obtain the SH electric fields radiated from the left and right sides of a multi-layered structure, containing N segments, by the following relation:

$$\begin{pmatrix} E_t^{(2)+} \\ 0 \end{pmatrix} = G_0^{-1} S_3^N G_0 \begin{pmatrix} 0 \\ E_r^{(2)-} \end{pmatrix} + \sum_{j=1}^{N} G_0^{-1} S_3^{N-j} \times \left\{ (B_M F_M - S_1 B_M) A_M \begin{pmatrix} \Omega_{3j}^{(1)+} \\ \Omega_{3j}^{(1)-} \end{pmatrix} + (1 - S_1) C_M \begin{pmatrix} \Omega_{3j}^{(1)+} \Omega_{3j}^{(1)-} \\ 0 \end{pmatrix} \right\}, \quad (21)$$

where $E_t^{(2)+}$ and $E_r^{(2)-}$ denote forward and backward SH electric fields, respectively. Forward and backward SHG efficiencies are defined as $\eta_F = \frac{|E_t^{(2)+}|^2}{|E_0^{(1)}|^2}$ and $\eta_B = \frac{|E_r^{(2)-}|^2}{|E_0^{(1)}|^2}$, respectively.

3 Numerical results and discussion

The intensity of incident FW of wavelength $\lambda = 810\,\text{nm}$ was set to $I_0 = 10\,\frac{\text{MW}}{\text{m}^2}$, corresponding to $|E_0| = 8.68 \times 10^4\,\frac{\text{V}}{\text{m}}$, to establish the undepleted pump approximation in all simulations. We assume the same thickness for air and SiO_2 layers ($d_A = d_S = d$) that can be changed in simulations while the thickness of MoS_2 mono layers are fixed at $d_M = 0.65\,\text{nm}$. Also the second-order susceptibility of MoS_2 mono layers was set as $\chi_M^{(2)} = 10^{-7}\,\frac{\text{m}}{\text{V}}$ and the second-order nonlinear optical coefficients of air and SiO_2 films were ignored in comparison with the MoS_2 coefficient [10–20].

Figure 3 shows the calculated forward and backward SHG efficiencies *versus* the same thickness of air and SiO_2 layers changing from 200 to 2000 nm for 1DNPC contains $N = 10$ segments. As shown in the figure, the SH efficiencies are enhanced in some thicknesses. The highest forward and backward efficiencies are equal to $\eta_F = 1.372 \times 10^{-5}$ and $\eta_B = 9.537 \times 10^{-6}$, respectively. The highest η_F occur when $d_A = d_S = 1285.73\,\text{nm}$ while the highest η_B is obtained at $d_A = d_S = 1285.17\,\text{nm}$.

As mentioned, the MoS_2 monolayers act as a source of SH waves in our structure. A SH wave generated in one layer travels to the other layers and can interfere with the new generated SH wave from secondary layers. As known,

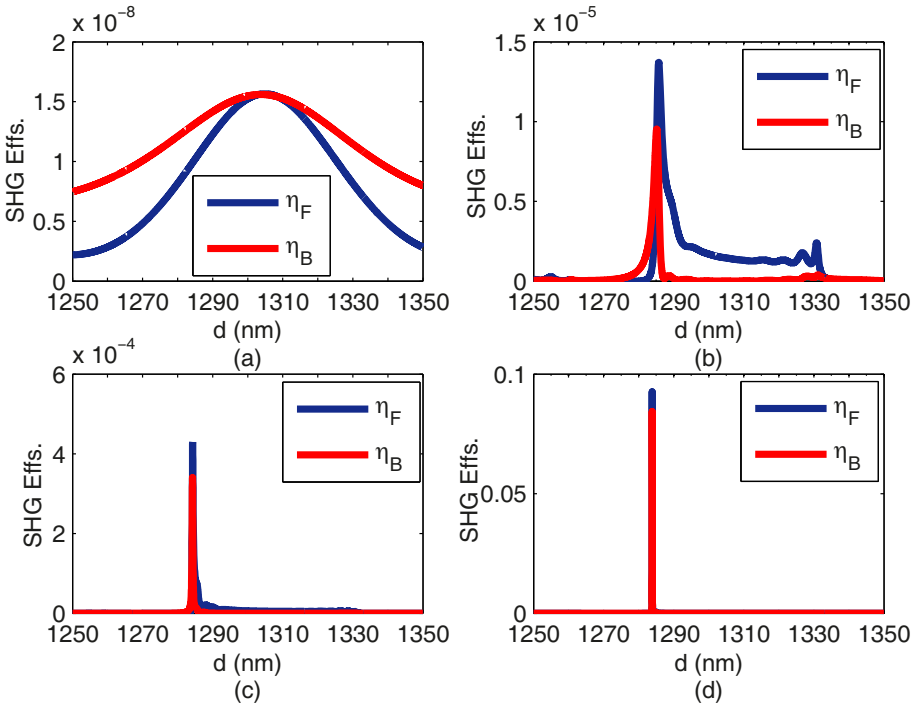

Fig. 4. Forward and backward SHG efficiencies *versus* the same thickness of air and SiO_2 layers for 1DNPC contains: (a) $N = 1$, (b) $N = 10$, (c) $N = 20$ and (d) $N = 40$ segments.

the interference can be constructive if the phase differences between all SH waves are an integer multiplication of SH wavelength ($\Delta\varphi = m\lambda_{\frac{1}{2}}$, m is an integer and $\lambda_{\frac{1}{2}}$ is SH wavelength). The main origin of the phase difference between two successive second harmonic generated wave source (MoS_2 monolayers) comes from the optical path length of SH wave between two MoS_2 monolayers and equals: $l_{OP} \approx (n_A + n_S(\lambda))d$, if we ignore the infinitesimal optical path length in the nonlinear layer. For highest efficiencies $l_{OP} \approx 9\lambda_{\frac{1}{2}}$, where $\lambda_{\frac{1}{2}} = 405\,\text{nm}$. It seems that the difference among all higher efficiencies comes from the effect of SH optical path length in the nonlinear layer which affects the waves interference.

At the next step we compared the SHG efficiencies in 1DNPC containing different numbers of segments. Figure 4 shows the results for $N = 1, 10, 20$ and 40 segments around $d = d_A = d_S = 1285\,\text{nm}$. As shown in this figure, the highest forward efficiencies are equal to 1.566×10^{-8}, 1.372×10^{-5}, 4.296×10^{-4}, 9.261×10^{-2} and the highest backward efficiencies equal to 1.560×10^{-8}, 9.537×10^{-6}, 3.403×10^{-4}, 8.428×10^{-2} in 1D photonic crystals contains $N = 1, 10, 20$ and 40 segments, respectively. The optimize thicknesses of air and SiO_2 layers of a structure, contains one segment, equal $d_f = 1304.89\,\text{nm}$ and $d_b = 1303.80\,\text{nm}$ for forward and backward SH waves, respectively. Also the optimized thicknesses of 1DNPC contains $N = 10$ segments equal $d_f = 1285.73\,\text{nm}$ and $d_b = 1285.17\,\text{nm}$, for $N = 20$ equal $d_f = 1284.28\,\text{nm}$ and $d_b = 1284.25\,\text{nm}$, for $N = 40$ equals $d_f = d_b = 1283.87\,\text{nm}$ for forward and backward SH waves, respectively.

The results show the giant enhancement of SHG efficiencies up to three order of magnitude in 1D photonic crystals contains sub wavelength MoS_2 monolayers including $N = 10$ segments and about seven order of magnitude for $N = 40$ segments with respect to $N = 1$. The results can be obtained by carefully tunning the thickness of air and SiO_2 layers to satisfy the phase matching conditions.

To more understanding the physics behind the enhancement of the second harmonic efficiencies, the transmission spectra of different engineered structures around the FW and SH wavelength are demonstrated in figs. 5 and 6, respectively. The figures show that both FW and SH waves are located at the photonic band gap edges for all engineered structures. As known at the photonic crystal band gap edges, the density of electromagnetic fields is large and the group velocity is low [30,31]. Therefore the field amplitudes can be enhanced and the nonlinear interaction time become much larger.

Benefit the phase matching conditions and the band gap tailoring causes the giant enhancement of second harmonic generation efficiencies in 1D photonic crystals contains 2D transition-metal dichalcogenide mono layers. It should be noted that the total width of a system contains $N = 40$ segments is about $102.73\,\mu\text{m}$ and the SHG efficiencies are near the 0.03 percent. Therefore it is expected that these small structures can be used as the nonlinear light sources.

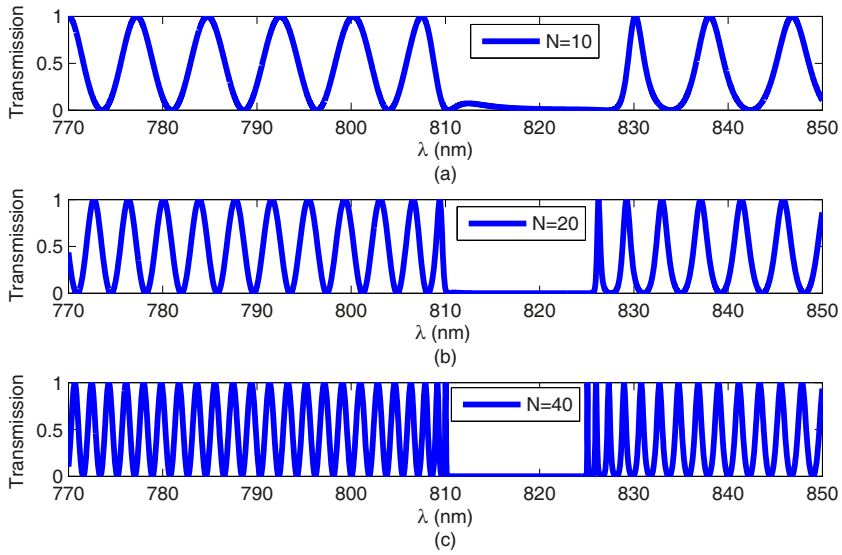

Fig. 5. Transmission spectra around the FW wavelength in 1DNPC contains: (a) $N = 10$, (b) $N = 20$, (c) $N = 40$ segments.

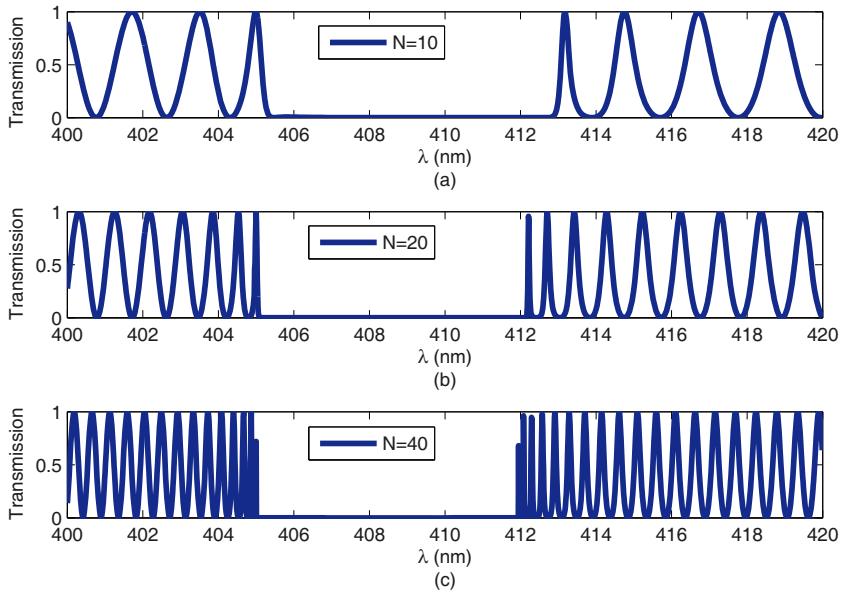

Fig. 6. Transmission spectra around the SH wavelength in 1DNPC contains: (a) $N = 10$, (b) $N = 20$, (c) $N = 40$ segments.

Figure 7 shows the SHG intensity *versus* the FW intensity in 1DNPC containing a different number of segments. Figures 7(a)–(d) indicate the quadratic dependence of SH to FW intensity. As known from eq. (9) the source of second harmonic wave depends quadratically to fundamental wave amplitude ($S \propto E_i^{(1)^2}$).

At the end, we investigated the optimal structure to reach the highest SH efficiencies by calculating the η_F and η_B *versus* the segment numbers. Figure 8 shows the results. The figure shows the highest efficiencies for each structure containing a different number of segments. As can be seen, the structure contains $N = 40$ segment (equal to $N = 40$ MoS_2 monolayers) and shows the highest SH efficiencies. Increasing the segment numbers above $N = 40$ diminished the SH efficiencies. We assumed the fixed thickness for MoS_2 monolayers ($d_M = 0.65\,\text{nm}$) in all simulations. At low segment numbers, the sub nano meter thickness of MoS_2 monolayers have no significant effects on phase matching conditions. Increasing the segments numbers enhanced the overall thickness (and optical path length of SH wave) of 2D nonlinear layers that affect the phase matching conditions and decreased the SH efficiencies.

In this experiment it is possible to realize the proposed air-gap photonic crystal in saw tooth structures. Our numerical results show that the optimal thickness of air and SiO_2 films are about 1300 nm or 1.3 μm. Therefore, it is possible to apply the nano or micro positioner to adjust the air gap thickness on the saw tooth structure. Also it

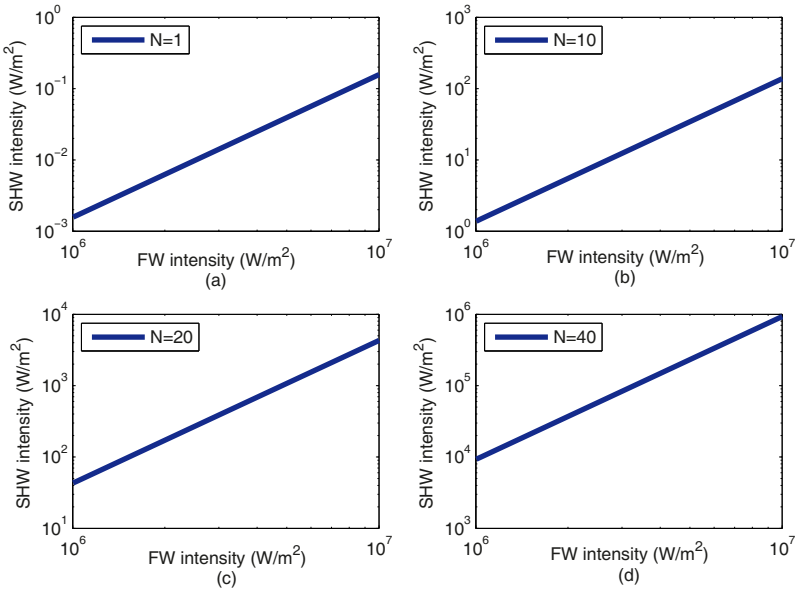

Fig. 7. Intensity dependence of forward second harmonic generation, with the solid line indicating the expected quadratic dependence.for 1DNPC contains: (a) $N = 1$, (b) $N = 10$, (c) $N = 20$ and (d) $N = 40$ segments.

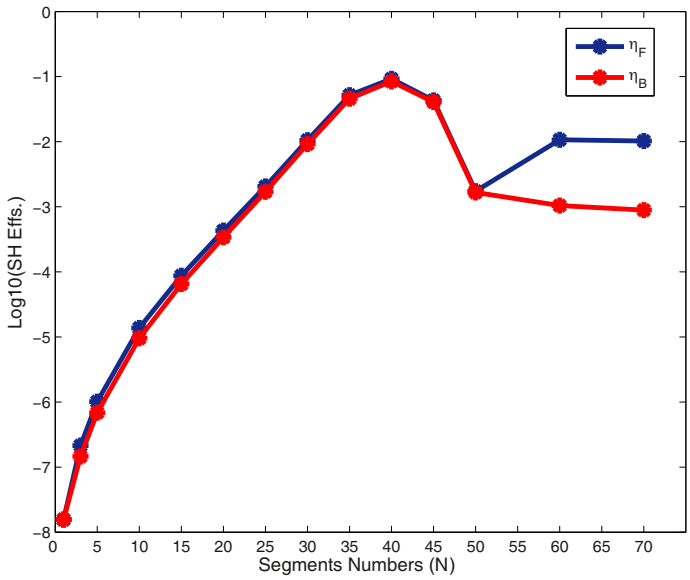

Fig. 8. Forward and backward SHG efficiencies *versus* the segment numbers (N) in logarithmic scale.

should be noted that it is straightforward to replace the air films with other materials such as Si, SiN, ZnS and TiO_2 with a determined dispersion relation in our calculations. We hope the structures can be used as a nonlinear light source to produce the coherent light wave at half wavelength.

4 Conclusion

The second harmonic generation efficiencies from finite 1D photonic crystal containing MoS_2 monolayers (as a two-dimensional transient metal dichalcogenide structures), air and SiO_2 films are calculated. We used the transfer matrix method in undepleted pump approximation for calculating the forward and backward second harmonic generation efficiencies. The enhancement up to the seventh order of magnitude is obtained for forward and backward second harmonic wave efficiencies in photonic crystals contain $N = 40$ segments. The results are obtained by carefully tuning the same thickness of air and SiO_2 layers at about 1284 nm for fundamental wave of $\lambda = 810$ nm wavelength. We utilize the phase matching and photonic band gap edge mechanisms to this end. Meanwhile, increasing the segment numbers, above $N = 40$, causes the increasing overall thickness of MoS_2 layers which destroyed the phase matching conditions and decreased the SHG efficiencies.

References

1. A.K. Geim, K.S. Novoselov, Nat. Mater. **6**, 183 (2007).
2. A.H.C. Neto, F. Guinea, N.M.R. Peres, K.S. Novoselov, A.K. Geim, Rev. Mod. Phys. **81**, 109 (2009).
3. K.F. Mak, C. Lee, J. Hone, J. Shan, T.F. Heinz, Phys. Rev. Lett. **105**, 136805 (2010).
4. K.F. Mak, J. Shan, Nat. Photon. **10**, 216 (2016).
5. Q.H. Wang, K. Kalantar-zadeh, A. Kis, J.N. Coleman, M.S. Strano, Nat. Nanotechnol. **7**, 699 (2012).
6. X. Hong, J. Kim, S.F. Shi, Y. Zhang, C. Jin, Y. Sun, S. Tongay, J. Wu, Y. Zhang, F. Wang, Nat. Nanotechnol. **9**, 682 (2014).
7. B. Mukherjee, F. Tseng, D. Gunlycke, K.K. Amara, G. Eda, E. Simsek, Opt. Mater. Express **5**, 447 (2015).
8. C. Yim, M. OBrien, N. McEvoy, S. Winters, I. Mirza, J.G. Lunney, G.S. Duesberg, Appl. Phys. Lett. **104**, 103114 (2014).
9. H. Zhang, Y. Ma, Y. Wan, X. Rong, Z. Xie, W. Wang, L. Dai, Sci. Rep. **5**, 8440 (2015).
10. N. Kumar, S. Najmaei, Q.N. Cui, F. Ceballos, P.M. Ajayan *et al.*, Phys. Rev. B **87**, 161403 (2013).
11. L.M. Malard, T.V. Alencar, A.P.M. Barboza, K.M. Mak, A.M.D. Paula, Phys. Rev. B **87**, 201401 (2013).
12. C. Janisch, Y.X. Wang, D. Ma, N. Mehta, A.L. Elias *et al.*, Sci. Rep. **4**, 5530 (2014).
13. X.B. Yin, Z.L. Ye, D.A. Chenet, Y. Ye, K. OBrien *et al.*, Science **344**, 488 (2014).
14. J.H. Zeng, M.H. Yuan, W.G. Yuan, Q.F. Dai, H.H. Fan *et al.*, Nanoscale **7**, 13547 (2015).
15. J.K. Day, M.H. Chung, Y.H. Lee, V.M. Menon, Opt. Mater. Express **6**, 2360 (2016).
16. G. Wang, X. Marie, I. Gerber, T. Amand, D. Lagarde *et al.*, Phys. Rev. Lett. **114**, 097403 (2015).
17. H. Zeng *et al.*, Sci. Rep. **3**, 1608 (2013).
18. Y. Li *et al.*, Nano Lett. **13**, 3329 (2013).
19. H. Chen, V. Corboliou, A.S. Solntsev, D.Y. Choi, M.A. Vincenti, D. De Ceglia, C.D. Angelis, Y. Lu, D.N. Neshev, Light: Sci. Appl. **6**, 17060 (2017).
20. J. Ribeiro-Soares, C. Janisch, Z. Liu, A.L. Elias, M.S. Dresselhaus, M. Terrones, L.G. Canado, G.A. Jorio, 2D Mater. **2**, 045015 (2015).
21. J.J. Li, Z.Y. Li, D.Z. Zhang, Phys. Rev. E **75**, 056606 (2007).
22. J. Li, Z. Li, Y. Sheng, D. Zhang, Appl. Phys. Lett. **91**, 022903 (2007).
23. M.L. Ren, Z.Y. Li, J. Opt. Soc. Am. B **27**, 1551 (2010).
24. S.M. Hamidi, T. Parvini, M.M. Tehranchi, Appl. Phys. A **111**, 525 (2013).
25. K. Sakoda, *Optical Properties of Photonic Crystals*, 2nd edition (Springer, 2004).
26. J.D. Joannopoulos, s.G. Johnson, J.N. Winn, R.D. Meade, *Photonic crystals: molding the flow of light* (Princeton University Press, Princeton, NJ, 2011).
27. C.M. Soukoulis, *Photonic crystals and light localization in the 21st century*, Vol. **563** (Springer Science and Business Media, Berlin, 2012).
28. T.K. Fryett, K.L. Seyler, J. Zheng, C.H. Liu, X. Xu, A. Majumdar, 2D Mater. **4**, 1 (2016).
29. G. Ghosh, Opt. Commun. **163**, 95 (1999).
30. Y. Dumeige, P. Vidakovic, S. Sauvage, I. Sagnes, J.A. Levenson, C. Sibilia, M. Centini, G. DAguanno, M. Scalora, Appl. Phys. Lett. **78**, 20 (2001).
31. J.M. Bendickson, J.P. Dowling, M. Scalora, Phys. Rev. E **53**, 4 (1996).